CHIN. PHYS. LETT. Vol. 38, No. 8 (2021) 084203 **Express Letter**

# PT Symmetry Induced Rings of Lasing Threshold Modes Embedded with Discrete Bound States in the Continuum

Qianju Song(宋前举)[1†], Shiwei Dai(戴士为)[1†], Dezhuan Han(韩德专)[1*], Z. Q. Zhang(张昭庆)[2], C. T. Chan(陈子亭)[2*], and Jian Zi(资剑)[3*]

[1]*College of Physics, Chongqing University, Chongqing 401331, China*
[2]*Department of Physics, Hong Kong University of Science and Technology, Clear Water Bay, Hong Kong, China*
[3]*Department of Physics, Key Laboratory of Micro- and Nano-Photonic Structures (MOE), and State Key Laboratory of Surface Physics, Fudan University, Shanghai 200433, China*

(Received 9 June 2021; accepted 19 July 2021; published online 3 August 2021)

It is well known that spatial symmetry in a photonic crystal (PhC) slab is capable of creating bound states in the continuum (BICs), which can be characterized by topological charges of polarization vortices. Here, we show that when a PT-symmetric perturbation is introduced into the PhC slab, a new type of BICs (*pt*-BICs) will arise from each ordinary BIC together with the creation of rings of lasing threshold modes with *pt*-BICs embedded in these rings. Different from ordinary BICs, the $Q$-factor divergence rate of a *pt*-BIC is reduced and anisotropic in momentum space. Also, *pt*-BICs can even appear at off-high symmetry lines of the Brillouin zone. The *pt*-BICs also carry topological charges and can be created or annihilated with the total charge conserved. A unified picture on *pt*-BICs and the associated lasing threshold modes is given based on the temporal coupled mode theory. Our findings reveal the new physics arising from the interplay between PT symmetry and BIC in PhC slabs.

DOI: 10.1088/0256-307X/38/8/084203

Bound states in the continuum (BICs) can be formed if symmetry mismatch exists between these states and the extended states in the environment. Thus, BICs do not couple to the extended waves even when they share the same frequencies and momenta. Examples in quantum mechanics were firstly given by constructing a local potential based on amplitude modulation of a free-particle wave function.[1,2] Since then, various mechanisms have been proposed to produce BICs in both quantum and classical waves.[3−23] For example, destructive interference of multiple resonance modes can provide the mechanism to create BICs.[3−5] From the topological viewpoint, BICs in photonic crystal (PhC) slabs can be characterized by the vortex centers of polarization vectors of far-field radiation.[7,8] BICs in 1D chain can also be characterized by the phase singularity of quasi-mode coupling strength.[9,10] Topological charges have been directly measured for the far-field polarization vectors in the momentum space.[11−15] It is worth noting that BICs are in fact the eigenstates with real eigenfrequencies of a non-Hermitian Hamiltonian.[4,5] Here, the non-Hermiticity is induced by the radiation loss of a system.[16−19] If there is intrinsic loss in the system, it only serves as a background so that the suppression of radiation loss still plays a key role in forming BICs.[12,20,21] In fact, non-Hermitian systems with PT symmetry have been extensively studied in the past decades.[24−27] Such systems can be achieved by introducing balanced gain and loss into otherwise Hermitian systems. An interesting phenomenon associated with such PT-symmetric systems is the existence of exceptional points at which the Hamiltonian becomes defective when some critical strengths of gain and loss are reached. As a result, its eigenstates coalesce and the eigenvalues undergo a transition from being real to complex pairs.[28−35]

Here, we study both numerically and analytically how BICs in a PhC slab are affected when a PT-symmetric perturbation is applied to the system. We are interested in the regime of small gain and loss so that the phenomena associated with the exceptional points will not arise. We find that each original BIC of the PhC slab will turn into a new type of BIC (*pt*-BIC) together with a ring of lasing threshold modes inside the Brillouin zone with the *pt*-BIC embedded in this ring. The region inside the ring is unstable and lasing will occur. Compared with the original BICs, the $Q$-factor divergence rate in the momentum space associated with the *pt*-BICs becomes reduced and anisotropic. Furthermore, the *pt*-BICs can exist away from the high-symmetry lines, whereas the original BICs always appear in high-symmetry lines. This striking property should be attributed to the PT sym-

Supported by the National Natural Science Foundation of China (Grant Nos. 12074049, 11727811, and 12047564), the Hong Kong Research Grants Council (Grant Nos. AoE/P-02/12, 16303119, and N_HKUST608/17), and the Fundamental Research Funds for the Central Universities (Grant Nos. 2020CDJQY-Z006 and 2020CDJQY-Z003).
†These authors contributed equally to this work.
*Corresponding authors. Email: dzhan@cqu.edu.cn; phchan@ust.hk; jzi@fudan.edu.cn
© 2021 Chinese Physical Society and IOP Publishing Ltd

metry. The *pt*-BICs can generate polarization vortices of the far-field radiation and, therefore, be characterized by topological charges. The evolution, generation and annihilation of *pt*-BICs with increasing strength of PT-symmetry are dictated by the conservation of topological charge.

To understand the physics of *pt*-BICs and lasing threshold modes, a unified picture based on the temporal coupled mode theory is developed.[36,37] From the coupled mode theory, the absorption and radiation rates, i.e., $\gamma_{\rm abs}$ and $\gamma_{\rm rad}$, can be used to characterize the resonance modes. A negative $\gamma_{\rm abs}$ denotes a net gain in the system. The difference between *pt*-BICs and lasing threshold modes can be manifested clearly in the $\gamma_{\rm abs}$–$\gamma_{\rm rad}$ plane. On the rings of lasing threshold modes, we have $\gamma_{\rm rad} = -\gamma_{\rm abs}$, indicating that the radiation loss is compensated by the net gain exactly. However, *pt*-BICs are special points on the ring at which both $\gamma_{\rm rad}$ and $\gamma_{\rm abs}$ are zero, indicating a state with no radiation or net gain/loss.

*Results.* The system under study is a PhC slab, which has a finite thickness in the $z$ direction. The system has a mirror symmetry about the $z = 0$ plane as shown in Fig. 1(a). If an incident electromagnetic wave is used to excite the guided resonance modes, a temporal coupled mode theory can be adopted to understand the spectral properties of this system.[36,37] We consider here a particular guided resonance mode of the PhC slab and two radiation channels: channels 1 and 2 from each side of the slab. We denote the amplitude and frequency of the resonance by $A$ and $\omega_0$, respectively. The two incoming waves with frequency $\omega$ are denoted by $s_{1,+}$ and $s_{2,+}$ respectively. The coupled mode theory gives

$$\frac{dA}{dt} = (-i\omega_0 - \gamma_{\rm rad} - \gamma_{\rm abs})A + \boldsymbol{\kappa}^{\rm T}\boldsymbol{s}_+, \tag{1}$$

where $\gamma_{\rm rad}$ and $\gamma_{\rm abs}$ are, respectively, the radiation and absorption rates, $\boldsymbol{s}_+ = \{s_{1,+}, s_{2,+}\}^{\rm T}$, and $\kappa = \{\kappa_1, \kappa_2\}^{\rm T}$ represents the coupling constants of the resonator to the two incoming waves. When gain and loss are introduced into the system, the value of $\gamma_{\rm abs}$ can be negative when the system has a net gain. The outgoing waves are related to the resonator and incoming waves through

$$\boldsymbol{s}_- = C\boldsymbol{s}_+ + \boldsymbol{D}A, \tag{2}$$

where $\boldsymbol{s}_- = \{s_{1,-}, s_{2,-}\}^{\rm T}$ stands for the two outgoing waves and $\boldsymbol{D} = \{D_1, D_2\}^{\rm T}$ denotes the corresponding coupling constants. The matrix $C$ represents the direct scattering and can be expressed by the direct reflection and transmission coefficients as follows:[36]

$$C = \begin{pmatrix} r_{\rm d} & t_{\rm d} \\ t_{\rm d} & r_{\rm d} \end{pmatrix}, \tag{3}$$

with $|r_{\rm d}|^2 + |t_{\rm d}|^2 = 1$ satisfying the conservation of energy flux. The energy flux conservation and time-reversal symmetry also give rise to

$$\boldsymbol{D}^+ \cdot \boldsymbol{D} = 2\gamma_{\rm rad}, \quad \boldsymbol{\kappa} = \boldsymbol{D}, \quad C\boldsymbol{D}^* = -\boldsymbol{D}. \tag{4}$$

Since the slab has the mirror symmetry about the $z = 0$ plane, the leakage into radiation channels 1 and 2 are either symmetric or antisymmetric, therefore one has $D_1 = \pm D_2$ for the coupling constants. Thus, the total scattering matrix that relates the incoming and outgoing waves by $\{s_{1,-}, s_{2,-}\}^{\rm T} = S\{s_{1,+}, s_{2,+}\}^{\rm T}$ can be obtained and expressed as

$$S = \begin{pmatrix} r_{\rm d} & t_{\rm d} \\ t_{\rm d} & r_{\rm d} \end{pmatrix} + \frac{\gamma_{\rm rad}}{-i(\omega - \omega_0) + \gamma_{\rm rad} + \gamma_{\rm abs}} \times \begin{pmatrix} -(r_{\rm d} \pm t_{\rm d}) & \mp(r_{\rm d} \pm t_{\rm d}) \\ \mp(r_{\rm d} \pm t_{\rm d}) & -(r_{\rm d} \pm t_{\rm d}) \end{pmatrix}. \tag{5}$$

Here the $\pm$ signs correspond to the even and odd resonance modes with respect to the mirror plane at $z = 0$.[36] The scattering matrix $S$ has a pole at $\omega = \omega_0 - i(\gamma_{\rm rad} + \gamma_{\rm abs})$ in the complex plane of $\omega$, known as a resonance.

The transfer matrix $M$, defined by $\{s_{2,+}, s_{2,-}\}^{\rm T} = M\{s_{1,+}, s_{1,-}\}^{\rm T}$, can be obtained from the scattering matrix $S$, and the matrix element $M_{22}$ has the expression

$$M_{22} = \frac{-i(\omega - \omega_0) + \gamma_{\rm rad} + \gamma_{\rm abs}}{t_{\rm d}[-i(\omega - \omega_0) + \gamma_{\rm abs}] + \gamma_{\rm rad}[t_{\rm d} \mp (r_{\rm d} \pm t_{\rm d})]}. \tag{6}$$

The zeros of $M_{22}$ for real $\omega$ are also called spectral singularities, which are certain points in the continuous spectrum that spoil the completeness of wave functions.[38–41] From Eq. (6), the spectral singularity exists only if $\gamma_{\rm rad} + \gamma_{\rm abs} = 0$ so that the radiation ($\gamma_{\rm rad} > 0$) is exactly balanced by the net gain in the system, leading to a purely real resonance frequency at $\omega = \omega_0$ with zero linewidth. Thus a zero of $M_{22}$ represents a lasing threshold of the system. In the absence of external source ($\boldsymbol{s}_+ = 0$), Eqs. (1) and (2) are reduced to $dA/dt = -i\omega_0 A$ and $\boldsymbol{s}_- = \boldsymbol{D}A$, respectively. The first equation implies that the amplitude of the mode is undamped, whereas the second equation implies a far-field radiation without any external source, which is a property of lasing. However, a special case arises when both $\gamma_{\rm rad}$ and $\gamma_{\rm abs}$ become zero. This is a state with neither absorption nor radiation loss, Eqs. (1) and (2) are reduced to two independent equations: $dA/dt = -i\omega_0 A$ and $\boldsymbol{s}_- = C\boldsymbol{s}_+$, which represent, respectively, an undamped resonator and the direct coupling of incoming and outgoing waves without the involvement of the resonator. Here, we call such states the *pt*-BICs.

Both 1D PhC and 2D PhC slabs support at-$\Gamma$ and off-$\Gamma$ BICs.[4] An at-$\Gamma$ BIC occurs when its symmetry forbids coupling with the external waves. The off-$\Gamma$ BICs are topologically protected and appear on

the high-symmetry lines of the Brillouin zone. A PhC slab without gain and loss is given as an example in Fig. 1(a). The PhC slab is periodic in the $x$ direction with period $a$, uniform in the $y$ direction and has a thickness of $h = 1.4a$ in the $z$ direction. The alternating dielectric layers have relative permittivities of $\varepsilon_1 = 4.9$ and $\varepsilon_2 = 1$ with widths of $d_1 = d_2 = 0.5a$. For the dielectric system considered here, we can ignore the intrinsic material loss in the study of BICs. For the PhC slab with a finite thickness, bands of guided resonances with finite lifetimes appear inside the light cone. Numerical analyses have been performed using COMSOL Multiphysics to obtain complex eigenfrequencies $\omega' + i\omega''$ for the guided resonances. The ratio $\omega'/2\omega''$ gives us the $Q$ factor. Here, we focus on the TE-like modes. This band, shown by the gray surface in Fig. 1(b), appears inside the light cone, and the $\boldsymbol{E}$ field is mostly parallel to the $x$–$y$ plane. Three BICs (black dots) with $\omega'' = 0$ occur at $k_x = 0$ and $\pm 0.164$ $(2\pi/a)$ on the $k_x$ axis. Such BICs are singularities of far-field polarization vectors, characterized by the quantized topological charges with their total charge conserved. These charges are marked by the black arrows in Fig. 1(a), indicating the directions along which the leakage is not allowed.

To introduce a PT-symmetric gain-loss modulation, we divide each unit cell into four layers of equal thickness and introduce gain or loss in each sublayer according to the order $\varepsilon_1' + i\varepsilon''$, $\varepsilon_2' - i\varepsilon''$, $\varepsilon_2' + i\varepsilon''$ and $\varepsilon_1' - i\varepsilon''$ so that the relation of PT symmetry $\varepsilon(x) = \varepsilon^*(-x)$ is satisfied as sketched in Fig. 1(c). We take $\varepsilon'' = 0.6$ as an example. The TE-like band is shown by the gray surface in Fig. 1(d). Strikingly, each ordinary BIC of the slab transforms into a ring of $\omega'' = 0$ as shown by the red lines in Fig. 1(d). On each ring, there exists one or several points which correspond to a new type of BIC (*pt*-BIC) as marked by black dots. The region inside the ring is unstable implying laser action. The analysis of these *pt*-BICs will be given in details later. We also note that, in the 1D system of periodic chain, solutions of $\omega'' = 0$ appear at some discrete points on the optical branch which are in the form of pair of *pt*-BIC and lasing threshold mode.[42] However, in PhC slabs here, it is remarkable to see that the lasing threshold modes now form continuous rings with *pt*-BICs embedded in them. It is well known that the ordinary BICs usually take place on the high-symmetry lines of the Brillouin zone since certain spatial symmetry can reduce the number of independent radiation channels. The classification of topological charges of the BICs on the high-symmetry lines has been given in Ref. [7]. Because of the breaking of inversion symmetry in the $x$ direction, the positions of three *pt*-BICs remain on the $k_x$ axis but are no longer symmetric. However, in addition to these three *pt*-BICs, a pair of *pt*-BICs are generated in the region away from the high symmetry lines (i.e., $k_x$ and $k_y$ axes) and located symmetrically with respect to the $k_x$ axis. The existence of *pt*-BICs at off-high symmetry lines should be attributed to the PT-symmetric perturbation.[7–9,11–15] We note that these newly generated *pt*-BICs also obey the law of the conservation of topological charge. Moreover, *pt*-BICs possess different scattering characteristics in their neighborhoods as compared with the ordinary BICs. For example, the $Q$ factor associated with each *pt*-BIC carries a reduced divergence rate and is anisotropic in momentum space as will be discussed in details later.

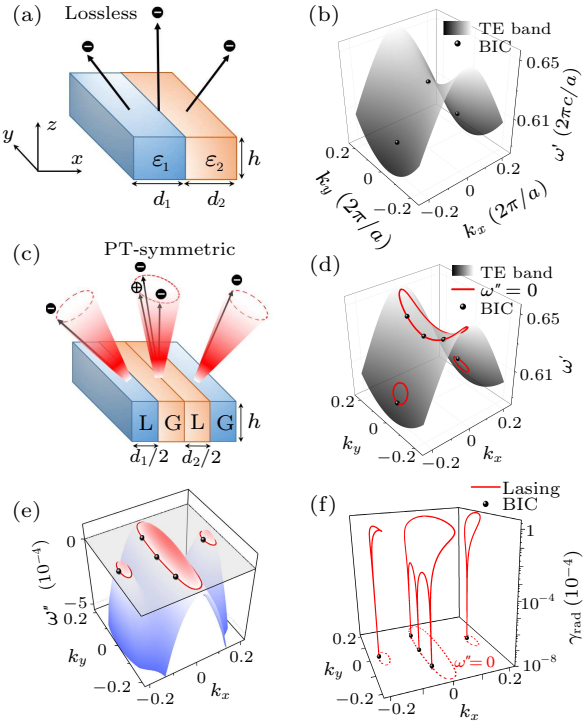


**Fig. 1.** Rings of lasing threshold modes spawning from the ordinary BICs. For a lossless PhC slab, (a) and (b) show three BICs (black dots) existing on the $k_x$ axis, corresponding to polarization vortices carrying topological charges; (c)–(f) are for a PT-symmetric PhC slab. Three rings with $\omega'' = 0$ (imaginary part of $\omega$) are shown by the red lines in (d) with *pt*-BICs embedded in these rings. A pair of *pt*-BICs are generated near the $\Gamma$ point but away from the high-symmetry lines. (e) $\omega''$ for the modes on the TE-like band, which is symmetric with respect to $k_x = 0$ and $k_y = 0$. Here $\omega''$ can be decomposed into $\gamma_{\rm rad} + \gamma_{\rm abs}$. (f) Radiation rate $\gamma_{\rm rad}$ for the modes with $\omega'' = 0$ (or $\gamma_{\rm rad} = -\gamma_{\rm abs}$) indicated by the red rings in (e). Black dots correspond to *pt*-BICs with $\gamma_{\rm rad} = \gamma_{\rm abs} = 0$; and the other modes with finite $\gamma_{\rm rad}$ correspond to lasing threshold modes at which the radiation loss is precisely balanced by the net gain. Here, the parameters are chosen as $\varepsilon_1 = 4.9$, $\varepsilon_2 = 1$, $d_1 = d_2 = 0.5a$, $h = 1.4a$, where $a$ is the lattice constant. For the PT-symmetric system, gain-loss modulation is introduced by $\varepsilon'' = \varepsilon''_{\rm loss} = -\varepsilon''_{\rm gain} = 0.6$ (imaginary part of $\varepsilon$).

In addition to *pt*-BICs, another type of possible solutions with real frequencies is the lasing threshold modes at which the radiation loss is precisely balanced by the net gain as mentioned in Eq. (6). Hence

all the other points on the rings of $\omega'' = 0$ except *pt*-BICs are lasing threshold modes. Although they are also eigenstates with real eigenfrequencies, these modes can radiate to the free space and, therefore, topological charge cannot be defined.

To reveal the underlying physics of the rings of singularities, we numerically evaluate the values of $\gamma_{\rm rad}$ and $\gamma_{\rm abs}$ in the following way. For any resonance modes, we can calculate their radiation power $P_{\rm rad}$, absorption power $P_{\rm abs}$ and the stored energy $U_{\rm eff}$. The decay rate due to radiative and non-radiative processes are defined by $\gamma_{\rm rad} = P_{\rm rad}/2U_{\rm eff}$ and $\gamma_{\rm abs} = P_{\rm abs}/2U_{\rm eff}$, respectively. Here a negative $\gamma_{\rm abs}$ represents the rate of power growth due to net gain in the system. The results are shown in Fig. S1 in the Supplemental Material, in which we found that the total decay rate $\gamma_{\rm tot} = \gamma_{\rm rad} + \gamma_{\rm abs}$ coincides with the imaginary part of the eigenfrequency $-\omega''$ of the resonance modes (also see Ref. [42]).

In Fig. 1(e), we also show the imaginary part $\omega''$ for the whole TE-like band. In spite of the breaking of inversion symmetry in the $x$ direction, $\omega''$ is still symmetric with respect to both the $k_y$ and $k_x$ axes in momentum space due to the spectral reciprocity along the $x$ direction and the spatial symmetry along the $y$ direction.[42,43] Three rings with $\omega'' = 0$ are shown in red, manifesting the zero total decay rate (or infinite lifetime) of the guided resonances. Each of these rings consists of either one or three discrete *pt*-BICs with $\gamma_{\rm rad} = \gamma_{\rm abs} = 0$ and continuous lasing threshold modes with $\gamma_{\rm rad} = -\gamma_{\rm abs} \neq 0$. Inside each ring, there exists an unstable lasing region marked in red color where $\omega'' > 0$, in which the energy of a resonant mode can grow exponentially in time. Although $\omega''$ is symmetric in the momentum space, the intrinsic properties of guided resonances can be characterized more clearly by decomposing $\omega''$ into two quantities: $\gamma_{\rm rad}$ and $\gamma_{\rm abs}$. The corresponding $\gamma_{\rm rad}$'s on the rings of $\omega'' = 0$ are shown in Fig. 1(f). The zeros of $\gamma_{\rm rad}$ represent the vanishing of far-field radiation, i.e., the existence of *pt*-BICs as indicated by the black dots. Thus, the numerical results shown here are consistent with the previous analysis in Eq. (6).

To be specific, the dispersion for the TE-like band with $\varepsilon'' = 0.6$ along the $k_x$ axis is shown in Fig. 2(a). The corresponding $\omega''$ is calculated numerically. The six singularities are marked by colored polygons at which $\omega'' = 0$. The presence of these singularities divides the $k_x$ axis into four stable passive regions with $\omega'' < 0$ and three unstable lasing regions with $\omega'' > 0$. The dispersion and the corresponding $\omega''$ for the guided resonances are symmetric with respect to the $\Gamma$ point. However, their hidden asymmetric features can only be seen clearly if we explore $\gamma_{\rm rad}$ and $\gamma_{\rm abs}$ separately for these modes. In Figs. 2(b) and 2(c), a $\gamma_{\rm rad} - \gamma_{\rm abs}$ plot for the negative and positive regions of $k_x$ are shown, respectively. The dashed line represents the zero total decay rate: $\gamma_{\rm tot} = \gamma_{\rm abs} + \gamma_{\rm rad} = 0$, or the condition of lasing threshold. It can be observed the locus of guided resonances in the $\gamma_{\rm rad} - \gamma_{\rm abs}$ plane intersects the dashed line. These six singularities are exactly the intersecting points, which fall into two classes: those with finite $\gamma_{\rm rad}$ and those at the origin with $\gamma_{\rm rad} = \gamma_{\rm abs} = 0$. The former corresponds to lasing threshold modes (red symbols), and the latter gives rise to *pt*-BICs (black symbols). We note that the absorption rate can take negative value in the PT-symmetric system due to the amplification from gain.[15] The spatial profiles of the field component $E_y$ at these six singularities are plotted in the insets of Fig. 2(a). The singularities with the same frequency but opposite $k_x$ possess completely different eigenstates: one of them is a *pt*-BIC with a spatially localized wave function, the other is a lasing threshold mode with a spatially extended wave function. It is interesting to see from Fig. 2(a) that PT-symmetric perturbation moves all ordinary BIC toward the $-k_x$ direction in momentum space as the strength of gain-loss modulation increases. This is different from the result of 1D periodic chain in which at-$\Gamma$ and off-$\Gamma$ BICs are shifted along the opposite directions.[42] Furthermore, the splitting of an ordinary BIC into a pair of *pt*-BIC and lasing threshold mode exists even if the PT-symmetric perturbation is very small as presented in Fig. S2 in the Supplemental Material.

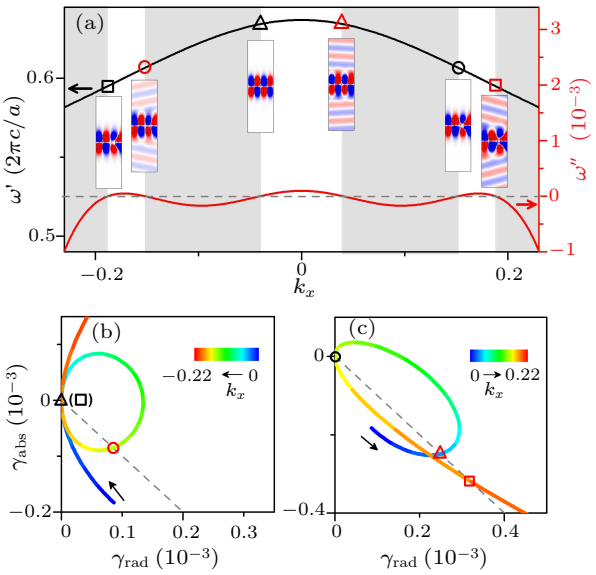


**Fig. 2.** (a) Simulated dispersion (black line) and the corresponding imaginary part $\omega''$ (red line) of a TE-like band along the $k_x$ axis for the PT-symmetric PhC slab with $\varepsilon'' = 0.6$. Insets of (a) show the simulated field profiles of $E_y$ at the six real-eigenfrequency states. The spatially localized (extended) ones corresponding to *pt*-BICs (lasing threshold modes) are labeled by the black (red) symbols. Absorption ($\gamma_{\rm abs}$) and radiation rate ($\gamma_{\rm rad}$) for these modes are shown in (b) and (c) along the negative and positive $k_x$ axes, respectively. The arrows indicate the directions of increasing $|k_x|$. The dashed lines represent the condition of $\gamma_{\rm abs} = -\gamma_{\rm rad}$.

The existence of lasing threshold modes leads to the division of momentum space into stable passive region and unstable lasing regions as shown in Fig. 3(a). The $Q$ factor of resonance modes in the neighborhood of a *pt*-BIC can be numerically calculated in the stable region. We take a *pt*-BIC at the point $(k_{x0}, k_{y0}) = (-0.040, 0)$ as an example, and consider the divergence rate of $Q$ factor along the dashed line with an included angle $\theta$ relative to the negative $x$ direction. We define $\delta k_x = k_x - k_{x0} = |\delta k| \cos\theta$ and $\delta k_y = k_y - k_{y0} = |\delta k| \sin\theta$. When $\theta = 0$, $\omega''$ tends to zero linearly in the stable region, i.e., $\omega'' \propto \delta k_x$ as seen in Fig. 2(a), therefore, the $Q$ factor diverges at the rate of $\delta k_x^{-1}$.[42] However, along the tangential direction of the ring ($y$ direction), the linear term vanishes and $\omega'' \propto \delta k_y^2$, leading to a $\delta k_y^{-2}$ divergent behavior of the $Q$ factor. Thus, a generic form of $Q$-factor divergence rate can be written as $Q \propto [c\delta k_x + \delta k_y^2]^{-1}$, where $c$ is a constant to be determined. By fitting the simulated $Q$ factor of resonance modes with this formula, the parameter is extracted as $c = 2.54$. The $Q$-factor divergence rate associated with a *pt*-BIC can be well approximated by this function, which is anisotropic in momentum space. This is distinct from the well-known behavior of $Q \propto \delta k^{-2}$[9,13,17] as well as the result of $Q \propto \delta k^{-1}$ found in 1D periodic chains.[42] All other *pt*-BICs have the similar anisotropic behavior as shown in Fig. S3.

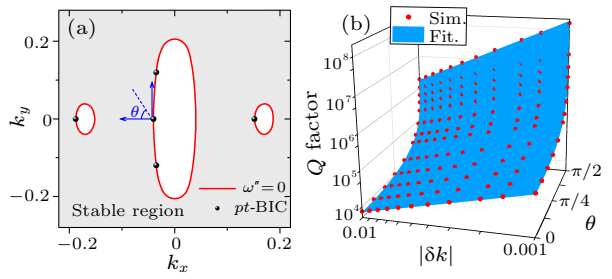


**Fig. 3.** (a) Three rings of lasing threshold modes (red lines) on the TE-like band and discrete *pt*-BICs (black dots) embedded in the rings. (b) The $Q$ factors of the guided resonances near a *pt*-BIC at $(k_{x0}, k_{y0}) = (-0.040, 0)$ are numerically calculated in the stable region (shaded in light gray) as shown by the red dots. The $Q$-factor divergence rate depends on the angle $\theta$ and is proportional to $[c\delta k_x + \delta k_y^2]^{-1}$ with $c = 2.54$ as shown by the blue sheet. For $\theta = \pi/2$, the $Q$ factor diverges at the rate of $\delta k_y^{-2}$, while at the rate is reduced to $\delta k_x^{-1}$ for $\theta = 0$, manifesting an anisotropic behavior in momentum space.

To study the effects of PT-symmetric perturbation on the topological charges characterized by the far-field polarization, we first project the far-field polarization onto the $s$–$p$ plane and then followed by a map onto the $x$–$y$ plane.[8] Previously, the far-field polarization is directly projected onto the $x$–$y$ plane.[7,11,12] However, the method of Ref. [8] can maintain the shape of the far-field polarization. We note that for a PhC slab the far-field polarization states are usually elliptical especially for the case without inversion symmetry. Moreover, the polarization vortices are not necessarily corresponding to BICs or *pt*-BICs, in some cases they come from the existence of circular polarization states (C points).[41–43] The difference is that polarization vanishes at BICs or *pt*-BICs but not at C points. It is therefore necessary to examine both the major axis $\boldsymbol{\alpha}$ and ellipticity for these polarization states, where $\boldsymbol{\alpha} = \alpha_x\hat{x} + \alpha_y\hat{y}$ represents the direction of the major axis, and $\rho_c = S_3/S_0$ with $S_0$ and $S_3$ being the first and fourth Stokes parameters. The nodal lines of $\rho_c$ shows the linearly polarized states, and the BICs or *pt*-BICs, as vortex singularities should occur at the crossing of two such nodal lines. However, the crossing of two such nodal lines does not necessarily lead to a BIC or *pt*-BIC if the polarization directions of these two nodal lines are not mutually orthogonal.

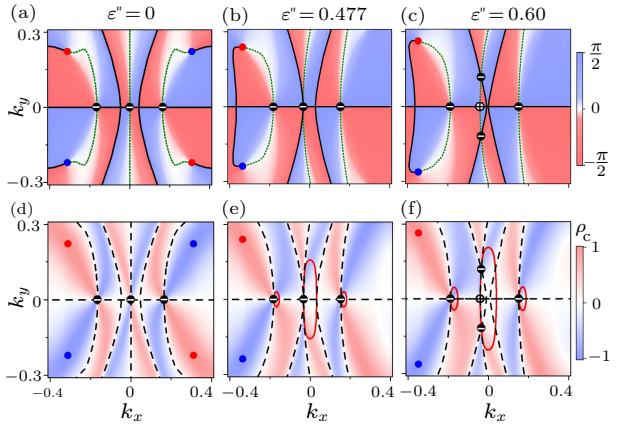


**Fig. 4.** Evolution of topological charges, and variations of the rings of lasing threshold modes together with the embedded *pt*-BICs when the strength of gain-loss modulation is increased. The directions of the projected far-field polarization vector $\boldsymbol{\alpha}$ are shown in (a)–(c). Nodal lines of $\alpha_x$ (black solid lines) and $\alpha_y$ (green dotted lines) are shown, in which the major axes are along the $y$ and $x$ directions, respectively. Each BIC or *pt*-BIC is a vortex center of polarization vector characterized by a topological charge. Two extra *pt*-BICs with $-1$ charge are generated when the value of $\varepsilon''$ is above a critical value $\varepsilon_c'' = 0.477$. Besides *pt*-BICs, there exist C points with 1/2 charge, marked by the red (blue) dots for the right-handed (left-handed) circular polarization. (d)–(f) Ellipticity $\rho_c$ of the elliptical polarization states. Linear polarization states ($\rho_c = 0$) are denoted by black dashed lines. Rings of lasing threshold modes ($\omega'' = 0$) are shown by the red lines. The BICs or *pt*-BICs are pinned on the linear polarization lines. Accompanied with each *pt*-BIC, a linearly polarized lasing threshold mode takes place at the same frequency but in the opposite $k_x$ space.

An example is given in Figs. 4(a) and 4(d) for the lossless system with $\varepsilon'' = 0$. Figure 4(a) shows the symmetries of the nodal lines of $\alpha_x$ (black solid lines) and $\alpha_y$ (green dotted lines) with respect to both the $k_x$ and $k_y$ axes due to the symmetry of the structure. Polarization vortices appear at the intersections of these two nodal lines when $\alpha_x = \alpha_y = 0$. The polarization vector $\boldsymbol{\alpha}$ falling in the 1st and 3rd (2nd and 4th) quad-

rants are shown in blue (red). Note that the quadrant of $\boldsymbol{\alpha}$ flips when any nodal line is crossed. Following a counterclockwise loop around a vortex, if $\boldsymbol{\alpha}$ rotates by an angle $-2\pi$, we can define that the vortex possesses a charge (or winding number) of $-1$. To examine the polarization states at the vortex centers, the ellipticity $\rho_c$ of polarization states are also shown in Fig. 4(d). It can be observed that linear polarization lines (black dashed lines) approach the nodal lines of $\alpha_x$ and $\alpha_y$ near the polarization vortices, indicating that the polarization states tend to be linear rather than elliptical and the polarization vortices should correspond to BICs instead of C points.

It is also worth mentioning that the far-field polarization of guided resonances in the PhC slab exhibits some remarkable features when the Bloch vector $\boldsymbol{k}$ is large. For instance, C points with 1/2 charge can be observed far away from the $\Gamma$ point as shown in Figs. 4(a) and 4(d). The red and blue dots correspond to the right-handed and left-handed circular polarizations, respectively. Distinct from the C points achieved by breaking the in-plane inversion symmetry of the PhC slabs,[44–46] Fig. 4(a) shows that C points can emerge even when the $C_2$ symmetry is maintained.

Since the rings of lasing threshold modes and the embedded *pt*-BICs appear immediately once a finite strength of gain-loss modulation is introduced into the system, the phenomena we have seen here are entirely different from those associated with the presence of exceptional points.[24–27] Figure 4 also shows the evolution of the rings of lasing threshold modes and topological charges at different values of $\varepsilon''$. In Figs. 4(b) and 4(c), the nodal lines of $\alpha_x$ (black solid lines) and $\alpha_y$ (green dotted lines) are shifted and deformed when the PT-symmetric perturbation is introduced. The original three intersection points of nodal lines with $\alpha_x = \alpha_y = 0$ still exist on the $k_x$ axis. When $\varepsilon''$ is increased from 0 to 0.477, the nodal lines of $\alpha_x$ and $\alpha_y$ near the middle *pt*-BIC moves towards each other. They finally touch each other when a critical $\varepsilon''_c = 0.477$ is reached, as illustrated in Fig. 4(b). As $\varepsilon''$ is further increased from 0.477 to 0.6, two more intersection points emerge and move away from the high-symmetry lines of momentum space (i.e., $k_x$ and $k_y$ axes), giving rise to two new polarization vortices. The charges of each vortex are indicated in Fig. 4(c). It is clearly seen that the total charge remains unchanged. From Fig. 4(f), it can be confirmed that the polarization states near these two vortices become linear, indicating that they correspond to *pt*-BICs instead of C points. These newly generated *pt*-BICs at off-high symmetry lines, appearing only above a critical strength of PT-symmetric perturbation, manifests the rich physics of evolution of BICs in PT-symmetric system which goes beyond the physics of exceptional points. Very recently, it was found that an off-high symmetry line BIC can also be produced by merging one Friedrich–Wintgen BIC with another accidental BIC with opposite charges.[47] However, such off-high symmetry line BICs are very different from the ones we discovered here. The off-high symmetry line *pt*-BICs shown in Figs. 4(c) and 4(f) are embedded in a ring of lasing threshold modes and carry a reduced and anisotropic $Q$-factor divergence rate.

Figures 4(e) and 4(f) also show the zeros of $\omega''$ for the resonance modes, which are three rings spawn from the three ordinary BICs in Fig. 4(d), consisting of the discrete points of *pt*-BICs and continuous lines of lasing threshold modes. Since the far-field polarization for the lasing threshold modes on these rings are not the vortex singularities, the radiation losses of these modes are exactly balanced by the net gain of the system. Moreover, for each *pt*-BIC, which can be either on the high-symmetry lines or off the high symmetry lines, there also exists a lasing threshold mode at the same frequency but with opposite $k_x$. It can be clearly seen in Fig. 4(f) that these accompanied lasing threshold modes are linearly polarized with zero ellipticity which are different from other lasing threshold modes on the ring. In other words, there is correspondence of linear polarization behavior between the states near *pt*-BICs and their accompanied lasing threshold modes in the opposite-$k_x$ space.

In summary, we have shown that when a PT-symmetric perturbation is added to a PhC slab, each existing BIC will turn into a ring of lasing threshold inside the Brillouin zone embedded with a new type of BIC (*pt*-BIC). This novel phenomenon partitions the Brillouin zone into stable passive regions and unstable lasing regions. The newly created *pt*-BICs are intrinsically different from the original BICs. They all carry a reduced and anisotropic $Q$-factor divergence rate and do not have to fall on the high symmetry lines. However, similar to the original BICs, *pt*-BICs can also be characterized by topological charges. The generation and annihilation of *pt*-BICs are governed by the conservation of topological charge. Our findings manifest the new physics arising from the interplay between BICs and PT-symmetry in PhC slabs. The creation of multiple unstable regions may also have potential applications in the PhC-based waveguides and lasers.

*Acknowledgement.* D. H. thanks L. Shi, C. Peng, C. X. Zheng and Mr. S. H. Du for helpful discussions.

## References

[1] von Neumann J and Wigner E 1929 *Phys. Z.* **30** 465
[2] Stillinger F H and Herrick D R 1975 *Phys. Rev. A* **11** 446
[3] Friedrich H and Wintgen D 1985 *Phys. Rev. A* **32** 3231
[4] Hsu C W, Zhen B, Stone A D, Joannopoulos J D and Soljačić M 2016 *Nat. Rev. Mater.* **1** 16048
[5] Koshelev K, Favraud G, Bogdanov A, Kivshar Y and Fratalocchi A 2019 *Nanophotonics* **8** 725
[6] Bulgakov E N and Sadreev A F 2011 *Phys. Rev. B* **83** 235321

[7] Zhen B, Hsu C W, Lu L, Stone A D and Soljačić M 2014 *Phys. Rev. Lett.* **113** 257401
[8] Yoda T and Notomi M 2020 *Phys. Rev. Lett.* **125** 053902
[9] Bulgakov E N and Maksimov D N 2017 *Phys. Rev. Lett.* **118** 267401
[10] Song Q, Zhao M, Liu L, Chai J, He G, Xiang H, Han D Z and Zi J 2019 *Phys. Rev. A* **100** 023810
[11] Doeleman H M, Monticone F, den Hollander W, Alù A and Koenderink A F 2018 *Nat. Photon.* **12** 397
[12] Zhang Y W, Chen A, Liu W Z, Hsu C W, Wang B, Guan F, Liu X H, Shi L, Lu L and Zi J 2018 *Phys. Rev. Lett.* **120** 186103
[13] Jin J, Yin X, Ni L, Zhen M S B and Peng C 2019 *Nature* **574** 501
[14] Wang B, Liu W, Zhao M, Wang J, Zhang Y, Chen A, Guan F, Liu X, Shi L and Zi J 2020 *Nat. Photon.* **14** 623
[15] Huang C, Zhang C, Xiao S, Wang Y, Fan Y, Liu Y, Zhang N, Qu G, Ji H, Han J, Ge L, Kivshar Y and Song Q 2020 *Science* **367** 1018
[16] Yuan L and Lu Y Y 2018 *Phys. Rev. A* **97** 043828
[17] Dai S W, Liu L, Han D Z and Zi J 2018 *Phys. Rev. B* **98** 081405(R)
[18] Gao X, Hsu C W, Zhen B, Lin X, Joannopoulos J D, Soljačić M and Chen H 2016 *Sci. Rep.* **6** 31908
[19] Bulgakov E N and Sadreev A F 2014 *Phys. Rev. A* **90** 053801
[20] Hsu C W, Zhen B, Lee J, Chua S L, Johnson S G, Joannopoulos J D and Soljačić M 2013 *Nature* **499** 188
[21] Liu Z, Xu Y, Lin Y, Xiang J, Feng T, Cao Q, Li J, Lan S and Liu J 2019 *Phys. Rev. Lett.* **123** 253901
[22] Tang H, DeVault C, Camayd-Muñoz S A, Liu Y, Jia D, Du F, Mello O, Vulis D I, Li Y and Mazur E 2021 *Nano Lett.* **21** 914
[23] Zhang M and Zhang X D 2015 *Sci. Rep.* **5** 8266
[24] Özdemir Ş K, Rotter S, Nori F and Yang L 2019 *Nat. Mater.* **18** 783
[25] El-Ganainy R, Makris K G, Khajavikhan M, Musslimani Z H, Rotter S and Christodoulides D N 2018 *Nat. Phys.* **14** 11
[26] Feng L, El-Ganainy R and Ge L 2017 *Nat. Photon.* **11** 752
[27] Miri M A and Alù A 2019 *Science* **363** eaar7709
[28] Bender C M and Boettcher S 1998 *Phys. Rev. Lett.* **80** 5243
[29] Feng L, Xu Y L, Fegadolli W S, Lu M H, Oliveira J, Almeida V, Chen Y F and Scherer A 2013 *Nat. Mater.* **12** 108
[30] Song W, Sun W, Chen C, Song Q, Xiao S, Zhu S N and Li T 2019 *Phys. Rev. Lett.* **123** 165701
[31] Yao S and Wang Z 2018 *Phys. Rev. Lett.***121** 086803
[32] Tang W, Jiang X, Ding K, Xiao Y X, Zhang Z Q, Chan C T and Ma G 2020 *Science* **370** 1077
[33] Zhen B, Hsu C W, Igarashi Y, Lu L, Kaminer I, Pick A and Soljačić M 2015 *Nature* **525** 354
[34] Zhu W, Fang X, Li D, Sun Y, Li Y, Jing Y and Chen H 2018 *Phys. Rev. Lett.* **121** 124501
[35] Luo J, Li J and Lai Y 2018 *Phys. Rev. X* **8** 031035
[36] Fan S, Suh W and Joannopoulos J D 2003 *J. Opt. Soc. Am. A* **20** 569
[37] Fan S and Joannopoulos J D 2002 *Phys. Rev. B* **65** 235112
[38] Longhi S 2010 *Phys. Rev. Lett.* **105** 013903
[39] Mostafazadeh A 2009 *Phys. Rev. Lett.* **102** 220402
[40] Longhi S 2010 *Phys. Rev. A* **81** 022102
[41] Mostafazadeh A 2011 *Phys. Rev. A* **83** 045801
[42] Song Q, Hu J, Dai S, Zheng C, Han D, Zi J, Zhang Z Q and Chan C T 2020 *Sci. Adv.* **6** eabc1160
[43] Zhou H, Zhen B, Hsu C W, Miller O D, Johnson S G, Joannopoulos J D and Soljačič M 2016 *Optica* **3** 1079
[44] Liu W, Wang B, Zhang Y, Wang J, Zhao M, Guan F, Liu X, Shi L and Zi J 2019 *Phys. Rev. Lett.* **123** 116104
[45] Yin X, Jin J, Peng M S C and Zhen B 2020 *Nature* **580** 467
[46] Chen W, Chen Y and Liu W 2020 *Laser Photon. Rev.* **14** 2000049
[47] Kang M, Zhang S, Xiao M and Xu H 2021 *Phys. Rev. Lett.* **126** 117402

# Supplemental Material for "PT Symmetry Induced Rings of Lasing Threshold Modes Embedded with Discrete Bound States in the Continuum"

Qianju Song(宋前举)[1,†], Shiwei Dai(戴士为)[1,†], Dezhuan Han(韩德专)[1,*], Z. Q. Zhang(张昭庆)[2], C. T. Chan(陈子亭)[2,*], and Jian Zi(资剑)[3,*]

[1] College of Physics, Chongqing University, Chongqing 401331, China

[2] Department of Physics, Hong Kong University of Science and Technology, Clear Water Bay, Hong Kong, China

[3] Department of Physics, Key Laboratory of Micro- and Nano-Photonic Structures (MOE), and State Key Laboratory of Surface Physics, Fudan University, Shanghai 200433, China

[*]Corresponding authors.

E-mail addresses: dzhan@cqu.edu.cn (D. Z. Han), phchan@ust.hk (C. T. Chan), and jzi@fudan.edu.cn (J. Zi)

[†] These authors contributed equally to this work.

## (I) The equality between $\gamma_{tot}$ and $-\omega''$

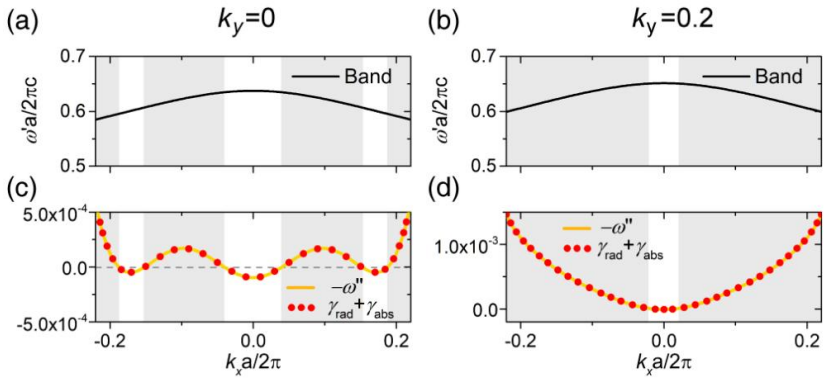


**Fig. S1.** Examples of simulated dispersion, imaginary part $\omega''$ and total decay rate $\gamma_{tot}=\gamma_{rad}+\gamma_{abs}$. The wave vectors are chosen $k_y$=0 and $k_y$=0.2 in the left and right panels, respectively. The total decay rate $\gamma_{tot}=\gamma_{rad}+\gamma_{abs}$ coincides with $-\omega''$.

In Fig. 1(e) of the main text, we only show the imaginary part of the eigenfrequency $\omega''$ and claim that total decay rate $\gamma_{tot}=\gamma_{rad}+\gamma_{abs}$ and $-\omega''$ of the resonance modes are coincident. Here, a numerical verification of $\gamma_{tot}$ always coincide with $-\omega''$ is shown in Fig. S1. We take the resonance modes on the TE-like band but with different wave

vectors as an example. Dispersion of TE-like band with $k_y$=0 and $k_y$=0.2 are shown in Figs. S1(a) and S1(b), respectively. In Figs. S1(c) and S1(d), we plot $-\omega''$ and the total decay rate $\gamma_{tot}$ of the resonance modes, which is coincides with each other.

**(II) *Pt*-BICs and lasing threshold modes at small PT-symmetric perturbation**

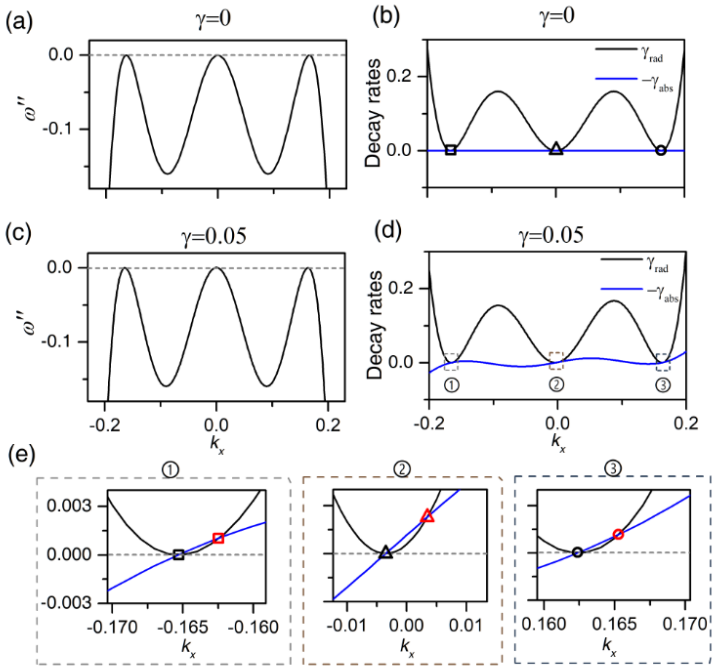


**Fig. S2.** Decay rates calculated from COMSOL Multiphysics. The imaginary part, absorption and radiation rate of resonance modes for $\gamma$=0 (a-b) and $\gamma$=0.05 (c-e). The intersections of curve $\gamma_{rad}$ and $-\gamma_{abs}$ with $\gamma_{rad}$=$\gamma_{abs}$=0 correspond to *pt*-BICs (black symbols). The other three with finite $\gamma_{rad}$ correspond to the lasing threshold modes (red symbols). Three zoom-in boxes in (e) correspond to the open rectangular regions shown in (d).

When a small PT-symmetric perturbation is introduced into the system, the splitting of an ordinary BIC into a pair of *pt*-BIC and a lasing threshold mode also exists. For a system without gain and loss, there exists three *pt*-BICs with $\omega''$=0 as shown in Fig. S2(a). The radiation rate $\gamma_{rad}$ is semi-positive definite and the absorption rate $\gamma_{abs}$ along the $k_x$ axis is always zero, therefore, $\gamma_{rad}$=0 correspond to BICs. When the system is perturbed by PT symmetry, $\gamma_{abs}$ fluctuates around zero along the $k_x$ axis. $\gamma_{abs}$ can intersect with the curves of $\gamma_{rad}$ at other three points as shown in Fig. S2(c-e), which is close to three BICs. The three intersections with $\gamma_{rad}$=$-\gamma_{abs}\neq$0 correspond to the lasing threshold modes (red symbols in Fig. S2(e)), at which the radiation loss is exactly balanced by the net gain.

**(III) Behaviors of Q factor near other *pt*-BICs**

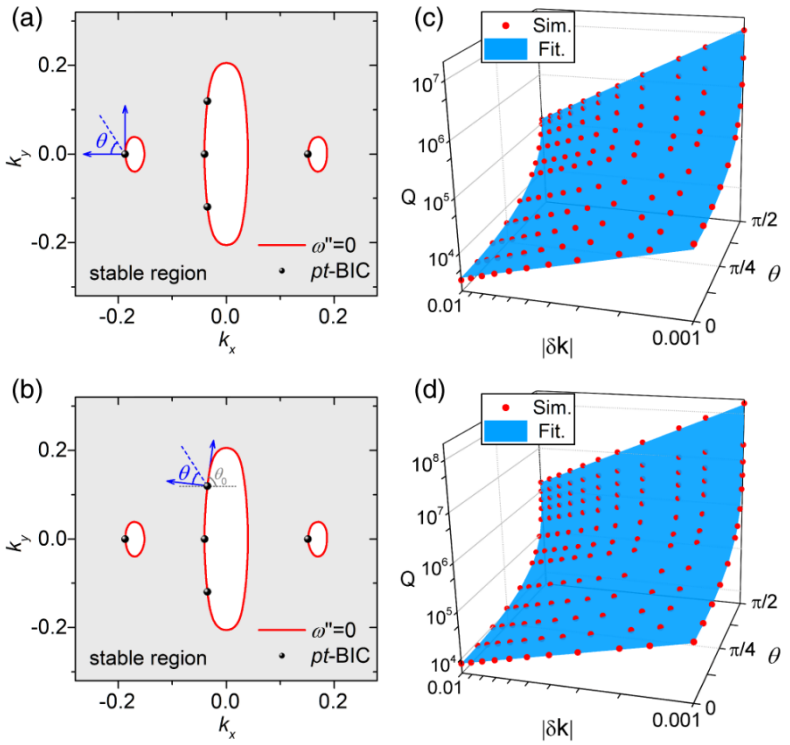


**Fig. S3.** (a-b) Lasing threshold modes (red lines) and *pt*-BICs (black dots) on the TE-like band as shown in the $k_x$-$k_y$ plane. The Q factors near *pt*-BICs point at ($k_{x0}$, $k_{y0}$)=(–0.188, 0) and (–0.035, 0.112) are shown in (c) and (d), respectively. (c) For $\theta=\pi/2$, the Q factor diverges at the rate of $\delta k_y^{-2}$, while at the rate of $\delta k_x^{-1}$ for $\theta=0$. (d) When the *pt*-BIC appear at off-high symmetry lines, the Q factor diverges at the rate of $[\delta k_x\cos\theta_0+\delta k_y\sin\theta_0]^{-2}$ along the tangential direction of the corresponding ring at the point of *pt*-BIC. The divergence rate of Q factor becomes $[-\delta k_x\sin\theta_0+\delta k_y\cos\theta_0]^{-1}$ along the normal direction ($\theta=0$).

Here, we also show the divergence behaviors of Q factor near the other *pt*-BICs. In Fig. S3(a), we take the *pt*-BIC point at ($k_{x0}$, $k_{y0}$)=(–0.188, 0) as the origin of coordinates and $\theta$ is the included angle between negative *x* direction and dashed line. For any arbitrary direction, we define $\delta k_x=k_x-k_{x0}=|\delta k|\cos\theta$ and $\delta k_y=k_y-k_{y0}=|\delta k|\sin\theta$. The Q factors along the dashed line with different included angle $\theta$ close to *pt*-BIC are shown in Fig. S3(c). For $\theta=0$, $\omega''$ crosses zero linearly near a *pt*-BIC and $\partial\omega''/\partial k_x$ is not zero. Therefore, $\omega''\propto\delta k_x$ and the Q factor is proportional to $\delta k_x^{-1}$. However, for $\theta=\pi/2$, the linear term vanishes and $\omega''\propto\delta k_y^2$, hence the Q factor carries a completely different Q-factor divergence rate, i.e., $Q\propto\delta k_y^{-2}$. The divergence rate of Q factor has the form of $[c\delta k_x+\delta k_y^2]^{-1}$, where *c* is a constant to be determined.

By fitting the simulated Q factor of resonance modes with this formula, we can extract the coefficient $c$=0.35.

The *pt*-BIC at off-high symmetry lines also holds similar anisotropic behavior. For convenience, we take the *pt*-BIC point at ($k_{x0}$, $k_{y0}$)=(−0.035, 0.112) as origin of coordinates as shown in Figs. S3(b). The tangential and normal directions of a ring of lasing threshold modes are defined as the coordinate axes of a local coordinate system. The local coordinate and the $k_x$-$k_y$ coordinate system can be linked by rotation operation and we obtain $\theta_0$=0.472$\pi$. The Q factors along the dashed line with different $\theta$ close to the *pt*-BICs are shown in Fig. S3(d). For $\theta$=$\pi$/2, the Q factor is proportional to $[\delta k_x \cos\theta_0 + \delta k_y \sin\theta_0]^{-2}$. For the other direction, the divergence rate of Q factor becomes $[-\delta k_x \sin\theta_0 + \delta k_y \cos\theta_0]^{-1}$. Thus, the divergence rate of Q factor has the generic form of $[c(-\delta k_x \sin\theta_0 + \delta k_y \cos\theta_0) + (\delta k_x \cos\theta_0 + \delta k_y \sin\theta_0)^2]^{-1}$, where $c$ is a constant to be determined. By fitting the simulated Q factor of resonance modes with this formula, we can extract the coefficient $c$=1.95.